Ab initio investigation of the magnetic and ferroelectric properties of BaCuF4 under hydrostatic pressure

D. Vincent, Xavier Rocquefelte, A. Saul

Ab initio investigation of the magnetic and ferroelectric properties of BaCuF$_4$ under hydrostatic pressure

David Vincent and Xavier Rocquefelte*

Univ Rennes, CNRS, ISCR (Institut des Sciences Chimiques de Rennes) UMR 6226, F-35000 Rennes, France

Andres Saúl

Aix Marseille Univ, CNRS, CINaM UMR 7325,
Campus de Luminy Case 913, 13288 Marseille, France

(Dated: October 3, 2022)

We present a first-principles investigation of the magnetic and ferroelectric properties of BaCuF$_4$. Our calculations indicate that the magnetic topology is one-dimensional, with a Néel temperature smaller than 1K, if existing. We also show that applying high pressure values up to 40 GPa on BaCuF$_4$ does not induce three-dimensional magnetic order. In addition, our calculations predict that the polar phase is destabilized under pressure. The first consequence is to reduce the energy barrier between $Cmc2_1$ polar and $Cmcm$ nonpolar phases, enhancing the ability to reverse the polarization. The second consequence is the disappearance of ferroelectricity above a critical pressure of 12.6 GPa.

I. INTRODUCTION

[1]The search of magnetoelectric materials, *i.e.* with coexisting magnetic and ferroelectric orders in the same phase [2, 3], is a hot topic for both academic and technological reasons. It represents a playground to study new physics and chemistry arising from the interplay between spin, charge, orbital and lattice degrees of freedom, and allows to imagine devices in which magnetism is controlled by electric fields and *vice versa*, paving the way of many innovative applications in spintronics [4] and data storage [5]. However, we are still far to reach the ideal multiferroic material, enabling a control of magnetism with low-energy electric field at room-temperature (RT) and with a high and switchable polarization. This technological bottleneck is directly related to the scarcity of multiferroics [6]. On the other hand, new routes have been proposed consisting to use epitaxial strain or high pressure to enhance or induce multiferroicity. Recently, it has been demonstrated that ferroelectricity can be induced by an epitaxial tensile strain in the ferromagnetic simple binary oxide EuO [7]. Similarly, we have demonstrated theoretically that under hydrostatic pressure CuO may reach RT functioning with an increase of the polarization [8, 9]. Kimura and coworkers have also shown that the orthorhombic phase of TbMnO$_3$ experiences a pressure-induced magneto-electric phase transition leading to a giant spin-driven ferroelectric polarization [10].

In 2018, a promising compound has emerged not from the oxide family but the fluorides [11]. Based on first-principles calculations, BaCuF$_4$ was shown to exhibit weak ferromagnetism coupled to ferroelectricity. The work claimed the existence of an unusually high Néel temperature T$_N$ of 275 K in spite that magnetic susceptibility and electron paramagnetic resonance experiments on powder samples [12] evidenced a one-dimensional (1D) antiferromagnetic behavior at high temperature and a ferromagnetic contribution below 20 K, that may be associated to the establishment of a three-dimensional (3D) order. A Néel temperature of about 275 K for a fluoride compound is surprising. First, BaCuF$_4$ belongs to a family of compounds BaMF$_4$ (with M = Mg, Mn, Fe, Co, Ni, Cu, and Zn), where the leading magnetic interactions of the other magnetic members (Mn, Fe, Co, Ni) are all antiferromagnetic (AFM) with long range magnetic order appearing at lower temperatures, *i.e.*, below 26.4, 54.2, 69.6, and 68.4 K for the Mn [13], Fe [14], Co [15], and Ni [16] compounds, respectively. Secondly, T$_N$ = 275 K is far above the largest T$_N$ value reported in the review article of J.F. Scott and R. Blinc on multiferroic fluorides [17], *i.e.* 148K for KMnFeF$_6$.

These challenging results motivated us to study the magnetic properties of this compound in more detail and to explore the influence of high pressure on its properties. In this paper, we show from first-principles calculations and Monte-Carlo (MC) simulations that BaCuF$_4$ is a pure one-dimensional antiferromagnet, without any signature of three-dimensional ordering (T$_N$ smaller than 1K). We also show that applying high pressure values up to 40 GPa on BaCuF$_4$ does not induce 3D magnetic order. In addition, our calculations predict that the polar phase is destabilized under pressure and the ferroelectric polarization disappears above 12 GPa.

This paper is organized as follows. In Section II, we discuss the methods that we used for the calculation of the electronic, magnetic and dynamical properties. In Sections III and IV, we present and discuss the predicted properties at ambient pressure and under hydrostatic pressure, respectively.

* xavier.rocquefelte@univ-rennes1.fr

II. CALCULATION METHODS

We performed density functional theory (DFT) calculations [18, 19] using the Vienna ab initio simulation package (VASP) [20] within the projector augmented plane wave (PAW) method [21–23]. We used the general-gradient approximation GGA-PBE parametrization [24, 25] for the exchange-correlation potential and PAW potentials with the valence electronic configurations $5s^2 5p^6 6s^2$ for Ba, $3d^{10} 4s^1$ for Cu, and $2s^2 2p^5$ for F. The localized d-electrons of copper were treated using GGA+U [26, 27] within the Dudarev formalism [28], with $U_{eff} = 8$ eV. The basis set was defined using plane-waves with a cutoff energy of 550 eV. A 24-atoms cell ($Cmc2_1$ unit cell) has been used for the geometry optimizations and the calculations of relative energies and ferroelectric polarization, and a 96-atoms cell (2a-b-2c supercell) for the magnetic properties. The k-mesh was converged depending on the calculated property ($6 \times 2 \times 5$ and $6 \times 4 \times 5$ for geometry optimization and accurate calculations, respectively) [29]. A tolerance of 10^{-6} eV was applied during the electronic minimisation, and the ion positions and lattice parameters were optimized until the magnitude of the forces on the ions was below 3.10^{-2} eV/Å.

The magnetic exchange interactions were estimated using the optimized atomic structures for each pressure (from 0 to 40 GPa), by mapping the computed magnetic spectra onto the energy spectra of an Heisenberg Hamiltonian:

$$\hat{H} = \hat{H}_0 + \sum_{i>j} J_{ij} \, \hat{S}_i \cdot \hat{S}_j, \qquad (1)$$

where $\hat{H}_0$ is the Hamiltonian independent of spin, J_{ij} the magnetic coupling between the magnetic sites i and j and $\hat{S}_i$ and $\hat{S}_j$ are the related quantum S = 1/2 spin operators. The broken symmetry method [30, 31] has been used to calculate the magnetic collinear coupling J_{ij} of the couple of magnetic sites ij [32–34]. The interaction between spins i and j can be evaluated from:

$$J_{ij} = E(\uparrow_i \uparrow_j) + E(\downarrow_i \downarrow_j) - E(\uparrow_i \downarrow_j) - E(\downarrow_i \uparrow_j) \qquad (2)$$

where $E(\sigma_i, \sigma_j)$ are the four spin configurations where the spins i and j take the values up or down while all the other spins are kept up. Hereafter, $J > 0$ indicates an antiferromagnetic (AFM) coupling, and $J < 0$ indicates a ferromagnetic (FM) coupling.

To estimate the spontaneous polarization, we computed the Born effective charges (BEC) [35] defined as:

$$Z_{ij}^* = \frac{\Omega}{e} \frac{\delta P_i}{\delta d_j} \qquad (3)$$

Where Ω is the volume of the system, e the elementary charge, i and j are directions of the displacement of an ionic sub-lattice. Integrating this expression one gets the spontaneous polarisation defined as the difference of polarization ΔP between polar (ferroelectric) and nonpolar

(paraelectric) phases:

$$P_s = \Delta P = \frac{e}{\Omega} \sum_i l_i \times \bar{Z}_i \qquad (4)$$

Where l_i is the displacement of the ion i and $\bar{Z}_i$ the average Born effective charge between these two phases. In the case of $BaCuF_4$, the ferroelectric and paraelectric phases are $Cmc2_1$ and $Cmcm$ respectively (see below).

The Murnaghan equation of state, which gives pressure (P) as function of volume (V), has been used to estimate the critical pressure P_c at the phase transition [36] :

$$P(V) = \frac{K_0}{K_0'} \left[\left(\frac{V}{V_0} \right)^{-K_0'} - 1 \right] \qquad (5)$$

where V_0, K_0 and K_0' are the equilibrium volume, the modulus of compressibility and its first derivative, respectively. Reversing the equation (5), allows us to derive an expression for the enthalpy $H(P) = U + PV$ as a function of P. The critical pressure P_c is obtained when the difference of enthalpies between two phases $\Delta H(P)$ is zero.

Lattice-dynamics calculations have been performed with the Phonopy package [37], via the supercell finite-displacement method [38]. A tolerance of 10^{-8} eV was applied during the electronic minimisation, and the ion positions and lattice parameters were optimized until the magnitude of the forces on the ions was below 10^{-3} eV/Å. We found that a supercell of 216 atoms ($3 \times 1 \times 3$ expansion) with a gamma-centered $2 \times 2 \times 2$ k-point grid allows to converge the shape of the phonon dispersion. From these data, an analysis of the dynamic stability of the polar and non-polar phases has been realized by checking the presence of imaginary modes.

To estimate the Néel temperature and the evolution of the magnetic properties with temperature, we have performed Monte-Carlo simulations implemented in the Algorithms and Libraries for Physics Simulations (ALPS) code [39]. We used the obtained J values from DFT calculations and a $S = \frac{1}{2}$ Heisenberg model. The simulations were performed with a cell containing 12288 magnetic sites, 250000 steps for the thermalization and 1500 Monte-Carlo steps per atom for the thermodynamic averages.

III. AMBIENT PRESSURE PROPERTIES

As mentioned above, $BaCuF_4$ belongs to a family of compounds $BaMF_4$ with M = Mg, Mn, Fe, Co, Ni, Cu, and Zn, which adopt a $Cmc2_1$[12] structure and are all polar. As shown in Figure 1 [40], $BaCuF_4$ can be described as layers of corner-sharing distorted CuF_6 octahedra, stacked along the **b** axis and separated to each others by Ba^{2+} ions.

Alternatively, the structure can be viewed as based on zig-zag chains of edge-sharing CuF_4 square-planar environments, oriented along the **c** axis. The optimized a,
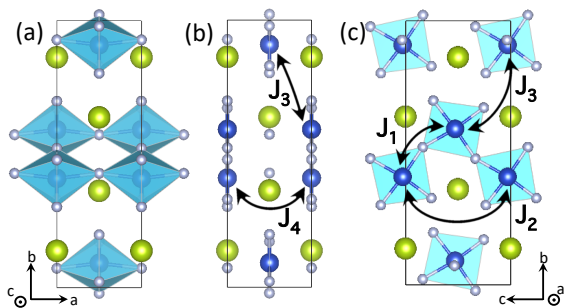
FIG. 1. Schematic representation of the $Cmc2_1$ ground state atomic structure of BaCuF$_4$. It can be described alternatively as constituted of layers of corner-sharing distorted CuF$_6$ octahedra (a) or zig-zag chains of corner-sharing CuF$_4$ square-planar environments (b and c). The magnetic exchange interactions are depicted. (All crystal visualization in this paper were performed using VESTA [40])

b and c cell parameters are 4.494, 14.208 and 5.661 Å, respectively, in good agreement with the experimental values (4.476, 13.972 and 5.551 Å) [12]. The Cu-F bond lengths in the equatorial plane are 1.6 % larger in average than the experimental ones, $i.e.$ 1.944 and 1.912 Å for relaxed and experimental mean distances, respectively. The longer apical Cu-F bond length is similar in the optimized and experimental structures (about 2.265 Å), confirming the distortion of the CuF$_6$ octahedra.

In order to investigate the magnetic properties of BaCuF$_4$, we have estimated the rotational invariant exchange interactions J_{ij} between the spin sites i and j using the procedure described in Section II. As shown in Figure 1, four different J_{ij} interactions can be defined, 2 intrachain (J_1 and J_2) and 2 interchain (J_3 and J_4). In the relaxed structure, the distance between the magnetic centers, $i.e.$ Cu-Cu bond length, is 3.836, 5.661, 5.783 and 4.494 for J_1, J_2, J_3 and J_4, respectively. J_1 is also defined by a Cu-F-Cu superexchange angle of 154°. J_2 and J_3 can be described by their Cu-F-F-Cu dihedral angles of 0 and 164°, respectively. J_4 corresponds to a coupling involving the apical F atom, with a Cu-F-Cu angle of 166°. The present GGA+U estimation of the magnetic couplings leads to $J_1 = 222$ K, $J_2 = 7$ K, J_3 = -2 K and $J_4 = 0$ K. It should be noticed that $J_4 = 0$ K is expected although the Cu-Cu distance and the Cu-F-Cu angles are favorable for a sizable AFM interaction. Indeed, each Cu^{2+} ion has only one magnetically active d$_{x^2-y^2}$ orbital which is in the (b,c) plane. As a consequence, the magnetic exchange interaction related to J_4, which is along the a direction (perpendicular to the magnetically active orbitals) is zero. It is interesting to note that in BaNiF$_4$, where the Ni^{2+} ions are in a 3d^8 electron configuration, the second magnetically active d$_{z^2}$ orbital is responsible of a J_4 effective interaction which is indeed larger than J$_1$ [41, 42] Similar values were obtained in Ref. [11], $i.e.$ $J_1 = 185$ K, J_3 = -0.4 and J_4 = -0.5 K (note that J_2 was not considered).

A rough estimate of J_1 can be obtained by comparing the experimental susceptibility, measured with a Faraday balance, to the magnetic susceptibility of a S = 1/2 AFM Heisenberg chain model [43] (see Figure 2):

$$\chi_{cal}^{CGS} = \frac{10^6 \ g^2 \mu_B^2 N_A}{4\pi \ J_1} \ \frac{d_{\text{eau}} \ m_{\text{material}}}{d_{solid}^{\text{material}} \ m_{\text{solution}}} \ \chi^* \quad (6)$$

Where χ^* is the calculated unitless susceptibility. The first part of the formula allows to convert the unit in CGS, $i.e.$ emu/Oe mol, with $g = 2.2$ the Landé factor, μ_B the Bohr magneton and N_A the Avogadro number. The second part of the formula allows to estimate the amount of magnetic particles in the solution, with d and m the densities and masses, respectively. The best fit is
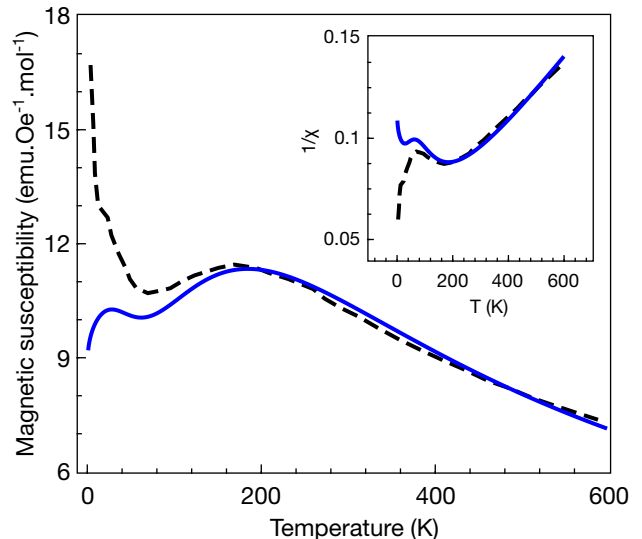

FIG. 2. The experimental (black dashed curve) magnetic susceptibility [12] is compared to a calculated one (blue solid curve) based on an S = 1/2 antiferromagnetic Heisenberg uniform chain model with J = 267 K [43]. The inset shows the corresponding inverse magnetic susceptibilities as a function of the temperature.

obtained for a mass percent of BaCuF$_4$ in solution of 8 % and $J_1 = 267$ K, which is close to the GGA+U estimation of 222 K. In addition, the estimated Curie-Weiss temperature is 431K, in close agreement with the experimental estimation of 430K, confirming that the magnetic topology is strongly one-dimensional with antiferromagnetic interactions. The disagreement at low temperature between the model and the experimental susceptibilities is certainly due to paramagnetic impurities in the sample.

Last but not the least, we have used the semi-empirical random phase approximation (RPA) expression, developed by Yasuda et $al.$ [44], for the estimation of T$_N$ for a quasi-1D AFM Heisenberg cubic lattice:

$$J' = \frac{T_N}{4c\sqrt{\ln(\frac{\lambda J}{T_N}) + \frac{1}{2}\ln(\ln(\frac{\lambda J}{T_N}))}} \quad (7)$$

where J and J' represent, respectively, the intra- and interchain magnetic couplings. J and J' were defined by comparing the energy expressions of the ground state magnetic order of $BaCuF_4$ ($E = J_1 - J_2 + 2J_3$) and of a quasi-1D antiferromagnetic Heisenberg cubic lattice ($E = J + 2J'$). It leads to $J = J_1 - J_2$ and $J' = J_3$. For c and λ parameters, we have used the values proposed in the original article of Yasuda *et al.* [44], *i.e.* $c = 0.233$ and $\lambda = 2.6$. Using the J_{ij} values previously calculated in GGA+U, it leads to T_N smaller than 1 K, far from the reported value of 275 K. Using these parameters, Kurzydlowski *et al.* systematically obtained larger T_N values than the experimental ones for quasi-one-dimensional spin-half copper fluoride antiferromagnets [45]. We thus expect an overestimated T_N value using equation 7.

In addition, by simulating the fourth order Binder cumulant U_L [46–48] defined as

$$U_L(T) = 1 - \frac{< m^4 >}{3 < m^2 >^2} \quad (8)$$

for a system of size L, where m is the magnetization of the system. When the value of $U_L(T)$ becomes different of zero for $T = T_c$, then we obtain the critical temperature T_c if L is large enough to approach the thermodynamic limit. However, no sign of a critical temperature in the range going from 1 to 300 K was found. All these results confirm the 1D character of the magnetic interactions in $BaCuF_4$ with no proof of the establishment of 3D magnetic order.

Concerning the ferroelectric properties at ambient pressure, we have estimated the spontaneous polarisation of $BaCuF_4$ using equation 4. The position of the ions on the path between the two phases were obtained using tools of the Bilbao crystallographic server. PSEUDO [49] was used to generate the Cmcm structure from the relaxed $Cmc2_1$ structure and AMPLIMODES [50, 51] to create the pathway between the two phases, which consists in a rotation of the CuF_6 octahedra, without any noticeable displacement of Cu and Ba atoms. This structural distortion can be associated to the instability evidenced by the imaginary modes in the phonon dispersion of the Cmcm phase (see below).

Figure 3a shows the energy well (energy difference between $Cmc2_1$ and $Cmcm$ phases) at ambient pressure and for P = 4 and 8 GPa. The related polarization, as function of the ferroelectric distortion, is also shown for P = 0 GPa (Figure 3b). Freezing values of -100, 0 and 100% correspond to octahedral rotation angles (Φ) of +12.7, 0 and -12.7° (black open circles), and spontaneous polarization (P_s) of -10.7, 0, +10.7 $\mu C.cm^{-2}$ (red diamonds), respectively. Such computed P_s values are very close to the ones obtained in Ref. [11]. At ambient pressure, $\Delta E = 68$ meV/f.u., which is in the range of the value calculated for $BaCoF_4$ ($\Delta E = 58$ meV/f.u. [41]), for which ferroelectric switching has been experimentally demonstrated [52]. It should be noticed that ΔE is twice larger than in [11]. To understand the possible origin
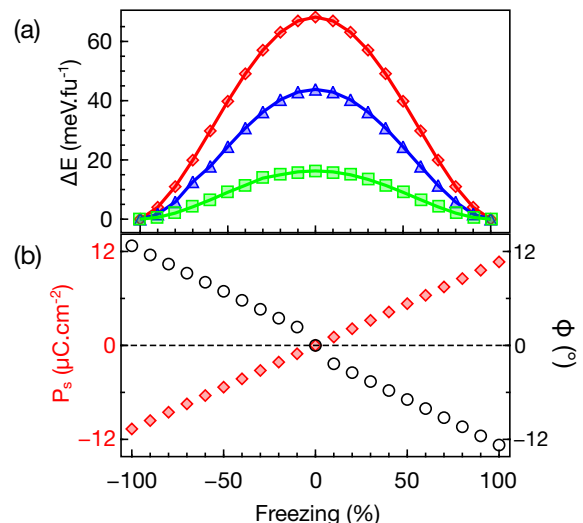

FIG. 3. (a) Double-well energy profile obtained by ferroelectric switching between positive and negative spontaneous polarization along the c axis for 0, 4 and 8 GPa, represented by red diamonds, blue triangles and green squares, respectively. (b) Spontaneous polarization reversal going from -10.7 to +10.7 $\mu C.cm^{-2}$ at 0 GPa, and octahedral rotation angle Φ, where a full octahedral reversal is observed.

of this difference we have tested the impact of changing the functional and the U_{eff} value. It shows that ΔE is reduced to 40 and 32 meV/f.u. when using PBE+U ($U_{eff} = 4$ eV) and PBEsol+U ($U_{eff} = 8$ eV), respectively. It confirms that ΔE value strongly depends on the functional and the U_{eff} value.

IV. EFFECT OF HYDROSTATIC PRESSURE

We will now consider the influence of applying an hydrostatic pressure on this compound. Figure 4 shows the evolution of the cell parameters under pressure, from 0 to 40 GPa. Our calculations evidence that the softest direction, *i.e.* with the largest relative compressibility, is the b axis, by a factor of 2 compared to a and c axes. From 0 to 12 GPa, the relative variation of the two hardest directions, a and c, are nearly the same, and for $P > 12$ GPa, a direction becomes smoother than c direction.

Such an ordering directly reflects the strength of the interactions which are stronger along c, *i.e.* the direction of the chains, than along a and b, which respectively correspond to the directions of the longer Cu-F bonds (Jahn-Teller distortion) and the stacking of the layers. The change of slope computed at about 12 GPa appears to be the signature of a structural transition from $Cmc2_1$ to $Cmcm$ phases.

To have a better estimate of the critical pressure (P_c), at which the nonpolar $Cmcm$ phase becomes more stable than the polar $Cmc2_1$ one, the Murnaghan equation of state (5) has been used. Figure 5 shows the evolution
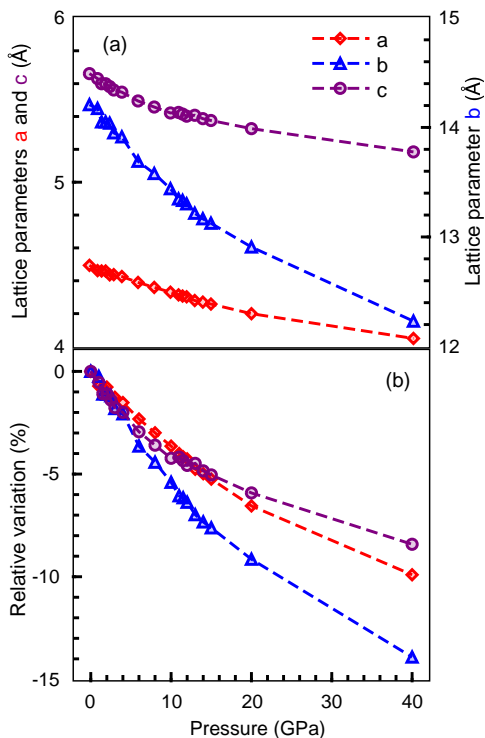
FIG. 4. (a) Calculated cell parameters of BaCuF$_4$ and (b) their relative variations under high pressure.

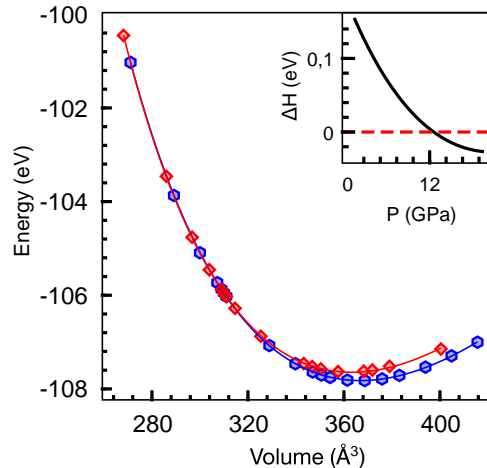FIG. 5. Energies of the polar (Cmc2$_1$), in blue hexagon, and non-polar (Cmcm), in red diamond, phases versus volume. The inset shows the calculated difference of enthalpies between the polar and nonpolar phase : $\Delta H = H_{Cmc2_1} - H_{Cmcm}$. A critical pressure appears at 12.64 GPa where the centrosymmetric phase becomes more stable than the polar phase.

of the total energy of each phase as a function of the cell volume under an applied hydrostatic pressure. The inset of Figure 5 gives the entalphy difference $\Delta H = H_{Cmc2_1} - H_{Cmcm}$ as a function of the applied pressure P. It allows to estimate a critical pressure $P_c = 12.64$ GPa.

Figures 6 shows the calculated phonon dispersions of the $Cmcm$ nonpolar phase for P = 0 and 8 GPa. While the computed phonon dispersions of the $Cmc2_1$ at 0 and 8 GPa do not show any imaginary modes, (Fig. S1 in the Supplementary Materials [53]), imaginary modes can be noticed along the way $\Gamma - \Sigma_0 - S - C_0 - Y - \Gamma$ at ambient pressure in the high-symmetry $Cmcm$ phase. It confirms its dynamical instability and evidences soft modes involving the cooperative rotation of the CuF$_6$ octahedra, leading to a transition towards the $Cmc2_1$ polar phase, which is the structural ground state from 0 to $P_c = 12.64$ GPa. In particular, when looking at the high-symmetry points, we found the following unstable modes: Γ_2^- at 62, S_2^+ at 53 and Y_2^- at 51 icm^{-1}, very close to the reported values [11]. These imaginary modes progressively disappear under pressure. As shown for P = 8 GPa, a small residue remains at the Γ point, and no more unstable modes are found at both S and Y points. The Γ_2^- mode is polar and is mainly based on the displacements of the F$^-$ ions, as depicted in Figure 7. It involves a ferrodistortive rotation of the CuF$_6$ octahedra around the $\boldsymbol{a}$ axis. The interpretation of the role of the Γ_2^- mode in the emergence of ferroelectricity can be understood us-

ing similar arguments than the ones used for the layered perovskite La$_2$Ti$_2$O$_7$ [54]. The crystallographic unit cell can be viewed as based on two $[Ba_2Cu_2F_8]$ $\boldsymbol{b}$-orientated slabs, each one containing two outer- and one inner-layers of fluorine atoms, respectively labeled F$_1$ and F$_2$. The displacement of F$^-$ ions in each $\boldsymbol{b}$-orientated layers give rise to an electric dipole along the $\boldsymbol{c}$ direction, $i.e.$ $\boldsymbol{p}_1$ and $\boldsymbol{p}_2$ dipoles, for F$_1$ and F$_2$ layers, respectively. The total dipole of a slab is then $\boldsymbol{p}_{slab} = 2\boldsymbol{p}_1 + \boldsymbol{p}_2$. Since no symmetry constraint exist between F$_1$ and F$_2$, the dipole of a slab will be non-zero. In addition, the amplitude of the movement is more than twice larger for F$_2$ than F$_1$ atoms. Finally, in the Γ_2^- mode, the two slabs of the unit cell exhibit identical collective displacements, giving rise to a net macroscopic polarization $P_s = 2p_{slab}$.

A deeper analysis of the structural evolution under pressure can be realized considering the variation of geometrical parameters (bond length and angle) between the magnetic sites. The evolution under pressure of the Cu-F-Cu angle and the Cu-Cu distance related to the largest coupling (J_1) is shown in Figures 8a and 8b.

While the Cu-Cu distance slightly decreases under pressure (from 3.84 to 3.77 Å), the Cu-F-Cu angle strongly increases (from 154 to 180°). Such an opening of the superexchange angle explains the increase of J_1 under pressure as illustrated in Figure 9a, which goes from 222 to 562 K, when P increases from 0 to 40 GPa. Figure 8c provides the variation under pressure of the Cu-Cu distance related to J_2. The Cu-Cu distance strongly decreases under pressure (from 5.7 to 5.2 Å), explaining the large increase of J_2 from 7 to 76 K, when P increases from 0 to 40 GPa. The two other couplings (J_3 and J_4) do not change significantly under pressure.
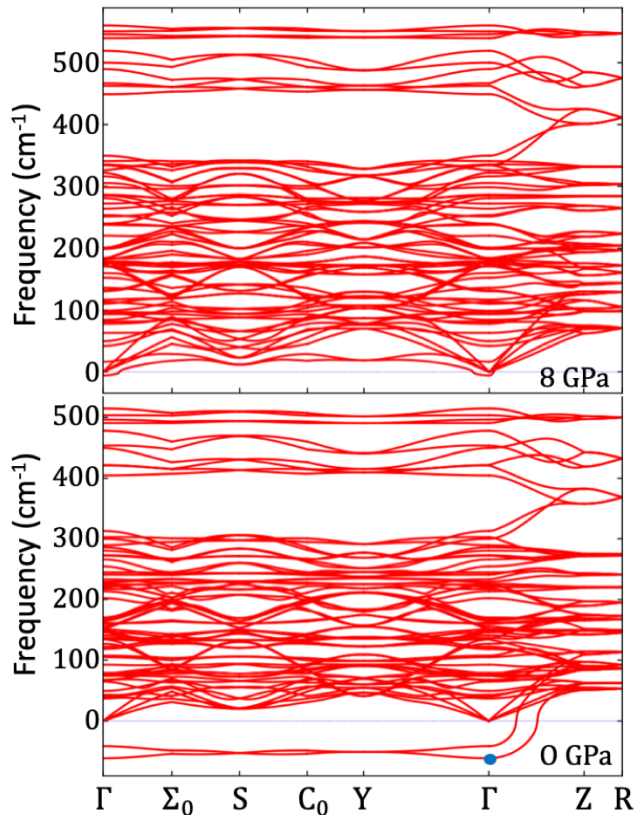
FIG. 6. Phonon dispersion curves of BaCuF$_4$ for phase Cmcm at 0 GPa (lower panel) and at 8 GPa (upper panel). Negative branches (*i.e.* imaginary and thus unstable modes) are observed and disappear under pressure. The Γ_2^- instability mode is highlighted by a blue dot.
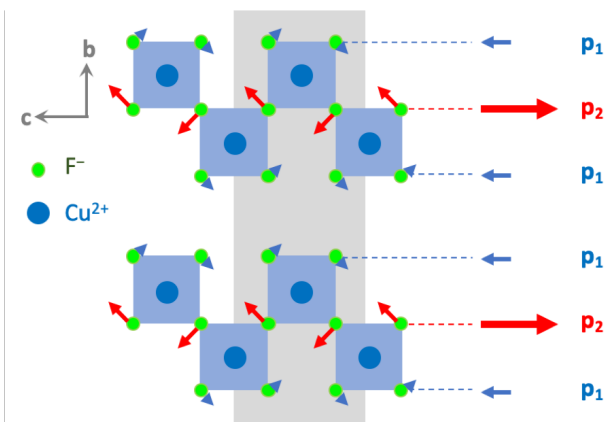

FIG. 7. Sketch of the largest atomic displacements associated to the Γ_2^- instability mode. The arrows on the right side represent the electric dipoles generated by the displacement of F$^-$ ions. One slab is composed of 3 layers of F$^-$ ions, stacked along the **b** axis. $\boldsymbol{p_1}$ and $\boldsymbol{p_2}$ dipoles arise from outer and inner layers, respectively. The crystallographic unit cell is represented by a grey rectangle. Ba atoms are not shown for simplicity.
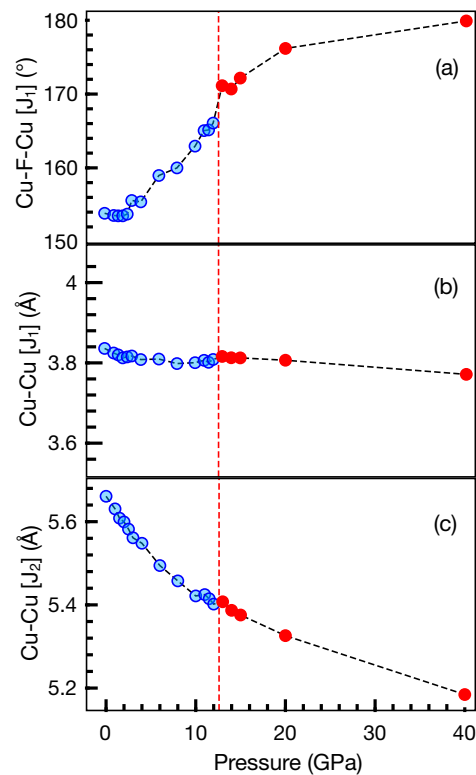

FIG. 8. Dependence of the structural parameters with applied pressure. (a) Super-exchange angle (Cu-F-Cu) and (b) Cu-Cu distance associated to the effective exchange interaction J_1. (c) Cu-Cu distance associated to the super-super-exchange interaction J_2. The effect of the pressure is more important on the super-exchange angle and the Cu-Cu distance associated to super-super-exchange. The critical pressure corresponding to the phase transition from $Cmc2_1$ to $Cmcm$ phases is depicted by a red dashed line. The points below (above) P$_c$ are represented in blue (red).

Using the so-obtained J values, we performed Monte-Carlo (MC) simulations to estimate the dependence of the magnetic susceptibility with temperature (Figure 9b):

$$\chi = \left.\frac{\partial M}{\partial H}\right|_{H=0} \propto \frac{< M^2 > - < |M| >^2}{k_b T} \qquad (9)$$

All the magnetic susceptibility curves have the same feature, which is characteristic of low-dimensional magnets. The maximum of the magnetic susceptibility is shifted towards higher temperatures under pressure, as expected from the increase of the J_1 value.

Finally, we have estimated the impact of the hydrostatic pressure on the ferroelectric properties. As expected, the energy barrier decreases with pressure with values of 68, 44 and 16 meV/f.u., respectively for P = 0, 4 and 8 GPa (Figure 3a). Such results evidences that (i) for $P < P_c$ the ferroelectric switching is easier under pressure and (ii) for $P > P_c$ the ferroelectricity vanishes. Indeed, Figure 10a shows the computed polarization (P_s) in the
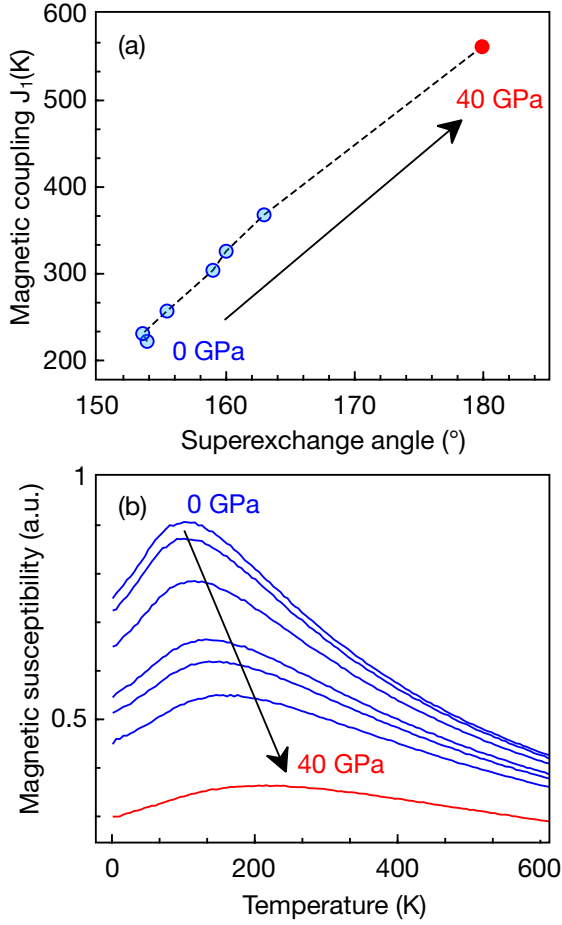
FIG. 9. (a) Dependence of the effective exchange interaction J_1 with the Cu-F-Cu superexchange angle. (b) Monte-Carlo simulations of the temperature dependence of the magnetic susceptibility for different values of hydrostatic pressure (P = 0, 2, 4, 6, 8, 10, 40 GPa). The gradual pressure increase is highlighted by an arrow in both panels.
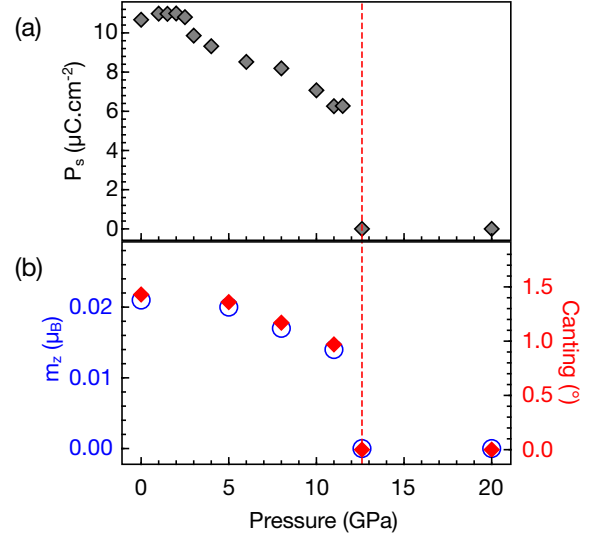

FIG. 10. (a) Pressure dependence of the spontaneous polarization calculated from the Born effective charges. At 12.6 GPa, a phase transition occurs from Cmc2$_1$ to Cmcm, leading to the disappearance of ferroelectricity. (b) Pressure dependence of the magnetic moment along the c axis (left axis) and the corresponding canting angle (right axis) obtained from the spin-orbit magnetic calculations (see text). The critical pressure is depicted by a red dashed line.

is responsible for the apparition of an additional AFM interaction along the a direction (J_4 in Fig. 1), leading to a 2D magnetic topology. Moreover, the single ion anisotropy permits the establishment of long range magnetic order at finite temperature, as observed experimentally below 70K [55]. In contrast, BaCuF$_4$ is essentially a 1D system where the anisotropy allows Ising-like AFM magnetic order at zero temperature with the magnetic moments oriented along the b axis. The small tilt associated with the canting is a consequence of the distortion of the Cmc2$_1$ polar phase and produces weak FM order along the c axis [11, 41, 42]. Interestingly, m_z decreases with pressure and vanishes at P = P$_c$ (see Fig. 10b) confirming the strong coupling between the weak-FM order and the electric polarization in BaCuF$_4$.

In conclusion, we have reconsidered the feasibility of multiferroicity close to room temperature in BaCuF$_4$ using first-principles calculations. The magnetic exchange interactions in BaCuF$_4$ evidence a 1D-topology, with a T$_N$ value smaller than 1K, if existing. Applying high-pressure reduces the energy barrier between polar and nonpolar phases, enhancing the ability to reverse the ferroelectric polarization. Above 12.6 GPa, the polar phase becomes unstable and a phase transition towards the nonpolar phase takes place with the loss of the ferroelectric polarization. It should be interesting to extend such an investigation to the other members of the family BaMF$_4$ where M is a transition metal (Fe, Mn, Cu, Ni, Zn, Mg).

ground state, which slightly increases from 0 to 2 GPa, reaching a value of $11\mu C.cm^{-2}$ and then decreases from 2 GPa to 11.5 GPa, reducing P_s by a factor of two. At about 12.6 GPa, the polar phase becomes unstable leading to a phase transition towards the non-polar Cmcm phase, and $P_s = 0$.

Figure 10b shows GGA+U calculations including spin-orbit to study the magneto-electric coupling in this system. Our calculations, at zero pressure, show a preference of the magnetic moments to lay along the b direction, with a small canting along the c axis (magnetic moment components of $m_x = 0$, $m_y = 0.844$ and $m_z = 0.021$ μ_B/Cu). Such results agree with the ones of Garcia Castro et $al.$ [11]. It should be noticed that similar results were reported by Ederer et $al.$ [41] and Leveque et $al.$ [42] for BaNiF$_4$, which is a S=1 system with Ni^{2+} ions in a 3d^8 electronic configuration. Interestingly, in BaNiF$_4$, the supplementary magnetic orbital

ACKNOWLEDGMENTS

[1] D. Vincent, X. Rocquefelte, and A. Saúl, Phys. Rev. B **106**, 064421 (2022).

[2] J. Young, A. Stroppa, S. Picozzi, and J. M. Rondinelli, Journal of Physics: Condensed Matter **27**, 283202 (2015).

[3] N. A. Benedek and C. J. Fennie, Phys. Rev. Lett. **106**, 107204 (2011).

[4] M. Fiebig, T. Lottermoser, D. Meier, and M. Trassin, Nature Reviews Materials **1**, 16046 (2016).

[5] A. Roy, R. Gupta, and A. Garg, Advances in Condensed Matter Physics **2012** (2012).

[6] N. Hill, Journal of Physical Chemistry B **104**, 6694 (2000).

[7] N. J. C. Ingle and I. S. Elfimov, Phys. Rev. B **77**, 121202 (2008).

[8] X. Rocquefelte, K. Schwarz, P. Blaha, S. Kumar, and J. Van Den Brink, Nature Communications **4**, 10.1038/ncomms3511 (2013).

[9] W. Lafargue-Dit-Hauret, D. Braithwaite, A. D. Huxley, T. Kimura, A. Saúl, and X. Rocquefelte, Phys. Rev. B **103**, 214432 (2021).

[10] T. Aoyama, K. Yamauchi, A. Iyama, S. Picozzi, K. Shimizu, and T. Kimura, Nature Communications **5**, 10.1038/ncomms5927 (2014).

[11] A. C. Garcia-Castro, W. Ibarra-Hernandez, E. Bousquet, and A. H. Romero, Phys. Rev. Lett. **121**, 117601 (2018).

[12] J.-M. Dance, Materials Research Bulletin **16**, 599 (1981).

[13] J. F. Scott, Reports on Progress in Physics **42**, 1055 (1979).

[14] M. Eibschütz, L. Holmes, H. J. Guggenheim, and D. E. Cox, Le Journal de Physique Colloques **32**, C1 (1971).

[15] M. Eibschütz, L. Holmes, H. J. Guggenheim, and D. E. Cox, Physical Review B **6**, 2677 (1972).

[16] W. Kleemann, F. J. Schafer, and J. Nouet, Journal of Physics C: Solid State Physics **14**, 4447 (1981).

[17] J. F. Scott and R. Blinc, Journal of Physics: Condensed Matter **23**, 113202 (2011).

[18] P. Hohenberg and W. Kohn, Phys. Rev. **136**, B864 (1964).

[19] W. Kohn and L. J. Sham, Phys. Rev. **140**, A1133 (1965).

[20] G. Kresse and J. Furthmüller, Phys. Rev. B **54**, 11169 (1996).

[21] P. E. Blöchl, Phys. Rev. B **50**, 17953 (1994).

[22] G. Kresse and D. Joubert, Phys. Rev. B **59**, 1758 (1999).

[23] D. Hobbs, G. Kresse, and J. Hafner, Phys. Rev. B **62**, 11556 (2000).

[24] J. P. Perdew, K. Burke, and M. Ernzerhof, Phys. Rev. Lett. **77**, 3865 (1996).

[25] J. P. Perdew, A. Ruzsinszky, G. I. Csonka, O. A. Vydrov, G. E. Scuseria, L. A. Constantin, X. Zhou, and K. Burke, Phys. Rev. Lett. **100**, 136406 (2008).

[26] H. J., Proc. R. Soc. Lond. A276238–257 **2012** (1963).

[27] A. I. Liechtenstein, V. I. Anisimov, and J. Zaanen, Phys. Rev. B **52**, R5467 (1995).

[28] S. L. Dudarev, G. A. Botton, S. Y. Savrasov, C. J. Humphreys, and A. P. Sutton, Phys. Rev. B **57**, 1505 (1998).

[29] H. J. Monkhorst and J. D. Pack, Phys. Rev. B **13**, 5188 (1976).

[30] C. Wüllen, The journal of physical chemistry. A **113**, 11535 (2009).

[31] H. Xiang, C. Lee, H.-J. Koo, X. Gong, and M.-H. Whangbo, Dalton Trans. **42**, 823 (2013).

[32] A. Saúl and G. Radtke, Physical Review Letters - PHYS REV LETT **106** (2011).

[33] D. Vaclavkova, A. Delhomme, C. Faugeras, M. Potemski, A. Bogucki, J. Suffczyński, P. Kossacki, A. R. Wildes, B. Grémaud, and A. Saúl, 2D Materials **7**, 035030 (2020).

[34] A. Saúl, N. Gauthier, R. M. Askari, M. Côté, T. Maris, C. Reber, A. Lannes, D. Luneau, M. Nicklas, J. M. Law, and et al., Physical Review B **97**, 10.1103/physrevb.97.064414 (2018).

[35] N. A. Spaldin, Journal of Solid State Chemistry **195**, 2 (2012), polar Inorganic Materials: Design Strategies and Functional Properties.

[36] F. D. Murnaghan, Proceedings of the National Academy of Sciences **30**, 244 (1944), https://pnas.org/content/30/9/244.full.pdf.

[37] A. Togo and I. Tanaka, Scripta Materialia **108**, 1 (2015).

[38] L. Chaput, A. Togo, I. Tanaka, and G. Hug, Phys. Rev. B **84**, 094302 (2011).

[39] B. Bauer, L. D. Carr, H. G. Evertz, A. Feiguin, J. Freire, S. Fuchs, L. Gamper, J. Gukelberger, E. Gull, S. Guertler, A. Hehn, R. Igarashi, S. V. Isakov, D. Koop, P. N. Ma, P. Mates, H. Matsuo, O. Parcollet, G. Pawłowski, J. D. Picon, L. Pollet, E. Santos, V. W. Scarola, U. Schollwöck, C. Silva, B. Surer, S. Todo, S. Trebst, M. Troyer, M. L. Wall, P. Werner, and S. Wessel, Journal of Statistical Mechanics: Theory and Experiment **2011**, P05001 (2011).

[40] K. Momma and F. Izumi, Journal of Applied Crystallography **41**, 653 (2008).

[41] C. Ederer and N. A. Spaldin, Physical Review B **74**, 10.1103/physrevb.74.024102 (2006).

[42] J. Lévêque, E. Rebolini, A. Saúl, and M.-B. Lepetit, The European Physical Journal B **94**, 214 (2021).

[43] D. C. Johnston, R. K. Kremer, M. Troyer, X. Wang, A. Klümper, S. L. Bud'ko, A. F. Panchula, and P. C. Canfield, Phys. Rev. B **61**, 9558 (2000).

[44] C. Yasuda, S. Todo, K. Hukushima, F. Alet, M. Keller, M. Troyer, and H. Takayama, Physical Review Letters **94**, 10.1103/physrevlett.94.217201 (2005).

[45] D. Kurzydłowski and W. Grochala, Phys. Rev. B **96**, 155140 (2017).

[46] K. Binder and D. Heermann, *Monte Carlo Methods in Statistical Physics* (Springer, 1979).

[47] K. Binder, Zeitschrift für Physik B Condensed Matter **43**, 119 (1981).

[48] K. Binder, Phys. Rev. Lett. **47**, 693 (1981).

[49] C. Capillas, E. S. Tasci, G. de la Flor, D. Orobengoa, J. M. Perez-Mato, and M. I. Aroyo, **226**, 186 (2011).

[50] D. Orobengoa, C. Capillas, and J. Perez-Mato, Journal of Applied Crystallography - J APPL CRYST **42**, 820 (2009).

[51] J. Perez-Mato and D. Orobengoa, Acta crystallographica. Section A, Foundations of crystallography **66**, 558 (2010).

[52] M. Eibschütz, H. Guggenheim, S. Wemple, I. Camlibel,

and M. DiDomenico, Physics Letters A **29**, 409 (1969).

[53] See Supplemental Material at `URL_will_be_inserted_by_publisher` for details.

[54] J. López-Pérez and J. Íñiguez, Phys. Rev. B **84**, 075121 (2011).

[55] D. E. Cox, M. Eibschütz, H. J. Guggenheim, and L. Holmes, Journal of Applied Physics **41**, 943 (1970).